GEOPHYSICAL RESEARCH LETTERS, VOL. ???, XXXX, DOI:10.1029/,

Sustained eruptions on Enceladus explained by turbulent dissipation in tiger stripes

Edwin S. Kite[1,2,3] & Allan M. Rubin[1]

[1]Department of Geosciences, Princeton University, Princeton, NJ 08542, USA.

[2]Department of Astrophysical Sciences, Princeton University, Princeton, NJ 08542, USA.

[3]Department of Geophysical Sciences, University of Chicago, Chicago, IL 60637, USA (kite@uchicago.edu).

Spacecraft observations suggest that the geysers on Saturn's moon Enceladus draw water from a subsurface ocean, but the sustainability of conduits linking ocean and surface is not understood. The prevailing view is that the 100km-long fissures ("tiger stripes") sourcing the geysers are clamped shut by tidal stresses for much of Enceladus' 1.3 day orbit, and that liquid-water conduits should freeze over within weeks, so that eruptions should be intermittent. However, observations show sustained (though tidally modulated) geysering throughout each orbit, and since the 2005 discovery of the plumes. Peak geyser flux lags peak tidal extension by ∼1 radian, suggestive of resonance. Here we show that a simple model of the tiger stripes as tidally-flexed slots that puncture the ice shell can simultaneously explain the persistence of the eruptions through the tidal cycle, the phase lag, the maintenance of fissure eruptions over geological timescales, and the total power output of the tiger stripe terrain. The delay associated with flushing and refilling of $O(1)$ m-wide slots with ocean water generates a phase lag relative to tidal forcing and helps to buttress slots against closure, while tidally pumped in-slot flow leads to heating and mechanical disruption that staves off slot freeze-out. Much narrower and much wider slots cannot be sustained. In the presence of long-lived slots, the 10^6-yr average power output of the tiger stripes is buffered by a feedback between ice melt-back and subsidence to ∼5 GW, which is equal to the observed power output, suggesting long-term stability. Turbulent dissipation makes testable predictions for upcoming flybys by

the *Cassini* spacecraft. Turbulent dissipation in long-lived slots helps maintain the ocean against freezing, maintains access by future Enceladus missions to ocean materials, and is plausibly the major energy source for tiger stripe activity.

1. Main text.

Enceladus' tiger stripes have been erupting continuously since their discovery in 2005 [*Porco et al.*, 2014; *Hansen et al.*, 2011; *Dong et al.*, 2011]. The eruptions have been sustained for much longer than that[1]: Saturn's E-ring, which requires year-on-year replenishment from Enceladus, has been stable since its discovery in 1966. Each of the four eruptive fissures is flanked by <1 km-wide belts of endogenic thermal emission (10^4 W/m for the $\sim$ 500 km total tiger stripe length), a one-to-one correspondence indicating a long-lived internal source of water and energy [*Nimmo & Spencer*, 2013]. The tiger stripe region is tectonically resurfaced, suggesting an underlying mechanism accounting for both volcanism and resurfacing, as on Earth. Enceladus' $\sim$35 km thick ice shell is probably underlain by an ocean or sea of liquid water [*Iess et al.*, 2014], and Enceladus' plume samples a salty liquid water reservoir containing ^{40}Ar, ammonia, nano-silica, and organics [*Postberg et al.*, 2011; *Waite et al.*, 2009]. A continuous connection between the ocean and the surface is the simplest explanation for these observations, but this leads to a severe energy-balance problem. The water table within a conduit would be $\sim$3.5 km below the surface (from isostasy), with liquid water below the water table, and rapidly ascending vapor plus entrained water droplets above. Condensation of this ascending vapor on the vertical walls of the tiger stripe fissures releases heat that is transported to the surface thermal-emission belts by conduction through the ice shell (Fig. 1) [*Abramov & Spencer*, 2009; *Porco et al.*, 2014; *Nimmo et al.*, 2014]. Because this vapor comes from the water table there is strong evaporitic cooling of the water table. This cannot be resupplied by thermal-convective exchange with the ocean unless the fissures are unrealistically wide

[*Postberg et al.*, 2009]. Freezing at the water table could release latent heat but would clog the fissures with ice in $\ll$1 yr. This energy deficit has driven consideration of shear-heating, intermittent eruptions, and heat-engine hypotheses [*Matson et al.*, 2012; *Nimmo et al.*, 2007; *Nimmo & Spencer*, 2013], but remains unsolved. It is easier to explain the observations if the heat is made within the plumbing system.

The observed long-term steadiness of ice and gas geysering is modulated (for ice) by fivefold variability at the period $p = 33$ hours of Enceladus' eccentric orbit about Saturn. Peak eruptive output anomalously lags peak tidal extension (by 5.1$\pm$0.8 hours relative to a fiducial model of the tidal response), and eruptions continue at Enceladus' periapse when all tidal crack models predict that eruptions should cease [*Porco et al.*, 2014; *Spitale et al.*, 2014; *Hurford et al.*, 2009; *Nimmo et al.*, 2014].

The sustainability of water eruptions on Enceladus affects the moon's habitability [*McKay et al.*, 2014], as well as astrobiology (follow-up missions to Enceladus could be stymied if the plumes shut down). Despite the importance of understanding the sustainability of the geysers, basic open questions remain: How can eruptions continue throughout the tidal cycle? Why is the total power of the system 5 GW (not 0.5 GW or 50 GW)? Do geyser mass and energy fluxes drive ice shell tectonics, or are the geysers a passive tracer of tectonics? How can the liquid water conduits stay open – as needed to sustain eruptions – despite evaporitic cooling and viscous ice inflow?

Here we show that a simple model of the fissures as open conduits can simultaneously explain both the diurnal phase curve of Enceladus' eruptions and the sustainability of eruptions on 10^{-1}–10^{6} yr timescales. Fissures are modeled as parallel rectangular slots with length L = 130 km, depth Z = 35 km, stress-free half-width W_0, and spacing S = 35 km. Slots are open to vacuum at the top, and open to an ocean at the bottom (Fig. 1, Supplementary Methods). Subject to extensional slot-normal tidal stress σ_n = (5±2) × 10^4 $\sin(2\pi t/p)$ Pa modified by elastic interactions between slots, the water table initially falls, water is drawn into the slots from the ocean (which is modeled as a constant-pressure bath), and the slots widen (Supplementary Materials). Wider slots allow stronger eruptions because the flux of a supersonic choked flow increases with nozzle width [*Schmidt et al.*, 2008]. Later in the tidal cycle, the water table rises, water is flushed from the slot to the ocean, the slot narrows, and eruptions diminish (but never cease). The slots never close completely because discharge is reduced as the slot narrows. $W_0 > 2.5$ m slots oscillate in phase with σ_n, $W_0 < 0.5$ m slots lag σ_n by $\pi/2$ rad, and resonant slots ($W_0 \sim 0.5$ m, tidal quality factor ~ 1) lag σ_n by ~ 1 radian (Fig. S4). The net liquid flow feeding the eruptions (<10 μm/s) is much smaller than the peak tidally-pumped vertical flow ($\sim \pm 1$ m/s for $W_0 \sim 1$ m).

Turbulent liquid water flow into and out of the slot generates heat. Water temperature is homogenized by turbulent mixing, allowing turbulent dissipation to balance water table losses and prevent icing-over. Ice forming at the water table is disrupted by aperture variations and vertical pumping A long-lived slot must satisfy the heat demands of evaporitic cooling at the water table (about 1.1× the observed IR emission; Methods) plus re-melting of ice inflow driven by the pressure gradient between the ice and the water in the slot [*Cuffey & Patterson*, 2010] (Supplementary Materials). Turbulent dissipation can balance this demand for W_0 = (1±0.5) m, corresponding to phase lags of 0.5-1 rad, consistent with observations. Eruptions are then strongly tidally-variable but sustained over the tidal cycle, also matching observations. W_0 <0.5 m slots freeze shut, and W_0 > 2.5 m slots would narrow. Near-surface apertures ∼10 m wide are suggested by modeling of high-temperature emission [*Goguen et al.*, 2013], consistent with near-surface vent flaring [*Mitchell*, 2005]. Rectification by choke points [*Schmidt et al.*, 2008], condensation on slot walls, and ballistic fall-back [*Postberg et al.*, 2011] could plausibly amplify the 2-fold slot-width variations in our model to the 5-fold variations in the flux of ice escaping Enceladus.[2] Water's low viscosity slows the feedback that causes the fissure-to-pipe transitions for silicate eruptions on Earth [*Bruce & Huppert*, 1989; *Wylie et al.*, 1999], which is suppressed for Enceladus by along-slot mixing (Supplementary Materials).

The mass and heat fluxes associated with long-lived slots would drive regional tectonics (Supplementary Materials). Slow inflow of ice into the slot [*Röthlisberger*, 1972] occurs predominantly near the base of the shell, where ice is warm and soft. Inflowing ice causes necking of the slot, which locally intensifies dissipation until inflow is balanced by melt-back. Melt-back losses near the base of the shell cause ice from higher in the ice shell to subside. Because subsidence is too rapid for conductive warming of the cold subsiding ice, subsidence of cold more-viscous ice is a negative feedback on the inflow rate. In equilibrium, the flux of ice consumed by melt-back near the base of the shell is equal to the flux of subsiding ice (Fig. S6), which in turn is equal to the mass added by condensation of ice from the vapor phase above the water table (Fig. S6). The steady-state flux of ice removed from the upper ice shell via subsidence and remelting at depth theoretically depends only on Z, S, moon gravity, and the material properties of ice, and is ∼1.5 ton/s (3 mm/yr, $Pe \approx 8$). This value, which is insensitive to reasonable variations in ice shell thickness and ice viscosity (Fig. 3, Fig. S7), is in exact agreement with the observed rate of ice *addition* to the upper ice shell, (4.6 ± 0.2) GW ≡ (1.6 ± 0.1) ton/s (assuming the observed IR cooling of the surface is balanced by re-condensation of water vapor on the walls of the tiger stripes above the water table; *Ingersoll & Pankine* [2010]; *Nimmo et al.* [2014]; *Nimmo & Spencer* [2013]). If near-surface condensates are distributed evenly across the surface of the tiger stripe terrain (either by near-surface tectonics [*Barr & Preuss*, 2010], or by ballistic fallback), then the balance is self-regulating because increased (decreased) tiger stripe activity will reduce (increase) the rate at which accommodation space for condensates is made available via subsidence in the near surface. This is consistent with sustained geysering on Enceladus at the Cassini-era level over $>10^6$ yr. Under these conditions the ice is relatively cold and nondissipative. In summary, turbulent dissipation of diurnal tidal flows (Fig. 1) naturally explains the interannual-to-decadal sustainability of liquid-water-containing tiger stripes (Fig. 2), and the coupling between long-lived slots and the ice shell forces a $>10^6$ yr geologic cycle that buffers Enceladus' power to ∼5 GW (Fig. 3).

Our model makes predictions for Cassini's flybys of Enceladus in late 2015 and early 2016. We predict that endogenic thermal emission will be absent between tiger stripes; the tiger stripes are the loci of sustained emission because other fractures are too short (L < 100 km) for sustained flow. Because sloshing homogenizes water temperatures along stripe strike (Supplementary Materials), there should be no correlation between the magnitude of emission and local tiger-stripe orientation, a prediction that distinguishes the slot model from all crack models. The slot model predicts a smooth distribution of thermal emission, in contrast to the spotty emission near jets that would be expected if flow is confined to pipes. The pattern of spatial variability should be steady, in contrast to bursty hypotheses (e.g. *Matson et al.* [2012]), and vapor flux should covary with ice-grain flux. Our simple model is a starting point for more sophisticated models of Enceladus coupling the liquid-dominated and gas-dominated parts of the conduits [*Ingersoll & Pankine*, 2010], as well as the tectonic evolution and initiation of the tiger stripe terrain (e.g., *Běhounková et al.* [2012]). Such coupling may be necessary to understand the initiation of ocean-to-surface conduits on ice moons including Enceladus and Europa, which remains hard to explain [*Crawford & Stevenson*, 1988; *Roth et al.*, 2014]. Initiation may be related to ice-shell disruption during a past epoch of high orbital eccentricity: such disruption could have created partially-water-filled conduits with a wide variety of apertures, and evaporative losses caused by geysering would ensure that only the most dissipative, with $W_0 = 1 \pm 0.5$ m, endure to the present day. Eccentricity variations on $\gg 10^7$ yr timescales may also be required if the ocean is to be sustained for the $\gg 10^7$ yr timescales that are key to habitability [*Meyer & Wisdom*, 2007; *Tyler*, 2011]. Ocean longevity could be affected by heat exchange with self-sustained slots in the ice shell. Testing habitability on Enceladus (or Europa) ultimately requires access to ocean materials, and this is easier if (as our model predicts) turbulent dissipation props the tiger stripes open for $\gg$Kyr.

Acknowledgments. We thank Or Bialik, Chris Chyba, Wim Degruyter, Shawn Ewald, Eric Gaidos, Terry Hurford, Leif Karlstrom, Michael Manga, Isamu Matsuyama, Karl Mitchell, Alyssa Rhoden, Max Rudolph, Britney Schmidt, Krista Soderland, Joseph

Spitale, Dave Stevenson, Robert Tyler, and Steve Vance; their contributions, ideas, discussion, and suggestions made this work a pleasure. We thank the scientific and local organizers of the Enceladus Focus Group meetings. This work was enabled by the U.S. taxpayer through grants NNX09AN18G, NNX09AL20G, and NNX11AF51G, and by a fellowship from Princeton University.

Appendix A: Supplementary Materials.

A1. Tidal stress cycle.

We calculate $\sigma_n(t, \phi, \theta)$ for Enceladus' tiger stripes (where ϕ is colatitude and θ is longitude) using a thin-shell approximation in which radial stresses are ignored, tiger stripes do not interact, and stresses due to physical libration, obliquity [*Hurford et al.*, 2009] and nonsynchronous rotation are assumed to be small [*Nimmo et al.*, 2007; *Smith-Konter & Pappalardo*, 2008; *Wahr et al.*, 2009]. We set the Poisson ratio for ice to 0.33 and use fiducial Enceladus degree-2 Love numbers $l_2 = 0.04$ and $h_2 = 0.2$ for ease of comparison with previous work (e.g., *Nimmo et al.* [2007]). High Love numbers are appropriate for a thin ice shell that is decoupled from the moon's rock interior by an ocean. Tiger stripe locations are hand-traced from sheet 15 of the 2010 controlled mosaic of Enceladus produced by the Deutsches Zentrum für Luft- und Raumfahrt (`http://photojournal.jpl.nasa.gov/catalog/PIA12783`), which incorporates the *Archinal et al.* [2011] longitude shift.

The results (Fig. S1) show that stresses along the tiger stripes are generally "in phase" (Fig. S2), with peak compression near periapse, and peak stresses along the main tiger stripes are also similar. Therefore we approximate the tiger stripes as straight, parallel, and with in-phase forcing. The peak-to-trough amplitude of the stress cycle along the main tiger stripes is ($1.31 \pm 0.28 \times 10^5$ Pa). Sensitivity tests introducing $< 90°$ phase lags between stripes show no significant effect.

A2. Slot width cycle.

Consider a thin shell of impermeable, isotropic ice I with thickness Z floating on a very voluminous water ocean. Stresses do not vary with depth within the ice shell, membrane stresses are neglected, and the ocean is treated as a constant-pressure bath. The shell is perforated by one or more rectangular slots of length L and (initially) uniform half-width W_0 ($L \gg W_0$), with walls of roughness k (Fig. S3). For the slot calculations we neglect curvature (adopting Cartesian geometry) and assume plane-stress. Plane-stress is more reasonable for Enceladus' tiger stripes than plane-strain: L = 90-190 km (from imaging), whereas Z is probably 30-40 km and very probably ≤ 60 km [*Iess et al.*, 2014].

Water rises within the slot to $D \approx \frac{\rho_i}{\rho_w} Z$, where $\rho_i = 916$ kg/m^3 is ice density and $\rho_w = 1000$ kg/m^3 is water density. Ocean over-pressure [*Rudolph & Manga*, 2009] or siphoning of the water by N_2 or CO_2 bubbles could raise the water table, but this would have only a small effect on our diurnal-cycle results. (Liquid water is not seen at the surface, suggesting that the ocean is not over-pressured by more than 0.3 MPa.) The slot is assumed to have adjusted prior to $t = 0$ through freezing and melt-back so that at $t = 0$ the slot width is uniform with depth.

The ice slab is subject to periodic, extensional, slot-normal stress $\sigma_n = \frac{A}{2}\sin(n_f t)$ where A is the peak-to-trough amplitude of the diurnal tidal stress cycle ($\sim 1.3 \times 10^5$ Pa for fiducial Enceladus l_2 and h_2), $n_f = 2\ \pi/p$, and $p \sim 33$ hours is the period of Enceladus' orbit. Sinusoidal time dependence is valid for small orbital eccentricity.

In the absence of water, and assuming linear elasticity, the plan-view slot area Y oscillates in phase with the forcing:

$$Y(t) = 2W_0L + \pi L \Delta W_m = L(2W_0 + \pi\sigma_n/E) \tag{A1}$$

where E is the Young's modulus of ice ($\sim 6 \times 10^9$ Pa [*Nimmo*, 2004; *Nimmo & Manga*, 2009]), and ΔW_m is the change in half-width at the location of greatest (maximum) half-width change. This is because $\Delta W = 2\ \sigma_n E^{-1}\sqrt{(L/2)^2 - y_*^2}$ where y_* is distance along-slot measured from the middle of the slot length [*Gudmundsson*, 2011].

Adding viscous fluid modifies the tidal cycle in Y. Conservation of water volume during a single tidal cycle relates changes in ΔW and volume exchange with the ocean:

$$\frac{\partial \Delta W_m}{\partial t}\left(\frac{\pi L}{2}\right)(D+h) + \frac{\partial h}{\partial t}\left(2W_0 + \frac{\Delta W_m \pi L}{2}\right) = Q \tag{A2}$$

where h is the time-varying part of the water level and Q corresponds to influx at the slot base. We assume $h \neq h(x)$, which is reasonable for Enceladus (§A.5-A.6). The first term on the left-hand side accounts for width change, and the second term accounts for changes in h. Slot-wall freeze-on and melt-back has characteristic timescale $\gg p$. h is set by the far-field stress σ_n as modified by the near-field elastic response to slot wall deformation:

$$\rho_w g h = -\frac{A}{2}\sin(n_f t) + \Delta W_m(t)\frac{2E}{L} \tag{A3}$$

where the water level responds to stress changes on timescale $\ll p$.[3] Differentiating,

$$\rho_w g \frac{\partial h}{\partial t} = n_f \frac{A}{2} \cos(n_f t) - \frac{\partial \Delta W_m(t)}{\partial t} \frac{2E}{L} \tag{A4}$$

Substituting,

$$\left(D + \frac{1}{\rho_w g} \left(-\frac{A}{2} \sin(n_f t) + \frac{\Delta W_m E}{L/2} \right) \right) \frac{\partial \Delta W_m}{\partial t} \left(\frac{\pi L}{2} \right) + \frac{1}{\rho_w g} \left(-n_f \frac{A}{2} \cos(n_f t) + \frac{\partial \Delta W_m}{\partial t} \frac{2E}{L} \right) \left(2 W_0 L + \frac{\pi L \Delta W_m}{2} \right) = Q \tag{A5}$$

Rearranging,

$$\frac{\partial \Delta W_m}{\partial t} = \frac{4 g \rho_w Q + 4 n_f L W_{0,i} (A/2) \cos(n_f t) + \pi n_f L \Delta W_m (A/2) \cos(n_f t)}{16 E W_{0,i} + 8 \pi E \Delta W_{m,i} - \pi L (A/2) \sin(n_f t) + 2 \pi g \rho_w D L} \tag{A6}$$

As a check we run $Q = 0$, $W_0 = 1$ m. This corresponds to a slot that contains water, but is hydrologically isolated from the ocean. We find $\Delta W_m \sim 0.02$ m, as expected, which would lead to negligible tidal flow within the slot, negligible viscous heat generation, and rapid shutdown of the eruption due to icing-over.[4]

Closure requires $Q(t) = Y(t)V(t)$ (V is velocity), but first we consider interactions between slots.

A3. Slot-slot interactions.

The tiger stripes are $S \sim 35$ km apart and $L \sim 130$ km long (stripes can be mapped using surface imagery or alternatively using the trace of individually triangulated supersonic ice sources; L is slightly shorter for the second approach), so elastic interactions between slots can be important. We model interactions using a two-dimensional displacement discontinuity implementation of the boundary element method [*Crouch & Starfield*, 1983;

Rubin & Pollard, 1988], with plane stress, neglecting planetary curvature. Using this code, we investigated interactions between slots of a variety of geometries, branching patterns, and lengths. The tiger stripes are reasonably well-approximated as being straight, parallel, equally spaced (Fig. S1) and in phase (Fig. S2). With those approximations, the tiger stripe terrain is symmetric, so that the deformation cycle for Alexandria and Damascus Sulci (the outboard slots) will be identical, and the deformation cycle for the Baghdad and Cairo Sulci (the inboard slots) will be identical. However, the deformation cycle for the outboard slots will differ from that for the inboard slots. Because slot width is much less than tiger-stripe spacing, the coupling terms are insensitive to both possible between-slot variations in mean width and possible along-slot variations in width.

With i as the perturbing stripe-pair and j as the perturbed stripe-pair, we can write the stress change that would occur on the walls of the perturbed stripe-pair if those walls were not free to move as follows:

$$\Delta P_{ji} = \frac{\Delta w_i}{\left(\frac{\partial w_i}{\partial p_i}\right)} \left(\frac{\partial w_j}{\partial p_i}\right) \left(\frac{\partial p_j}{\partial w_j}\right) = \left(\frac{\partial p_{j,iso}}{\partial w_{j,iso}}\right) r_{ij} \Delta W_{m,i} \qquad \text{(A7)}$$

where the subscript *iso* corresponds to deformation of a *single* slot of length equal to j.($\partial p_{iso}/\partial w_{iso} = 2E/L_{ts}$ for a straight slot.) Δw_i is found iteratively and all other terms are pre-computed using the two-dimensional displacement-discontinuity boundary element code. Elastic interactions are rapid relative to the tidal cycle (the sound-crossing timescale $(3S/v_{sound}) = (10^2$ km/4 km/s$) \approx 30$ s $\ll p$).

Taking account of perturbation by the other three slots, (A6) becomes

$$\frac{\partial \Delta W_{m,i}}{\partial t} = \frac{4g\rho_w Q + 4n_f L W_{0,i}(A/2)\cos(n_f t) + \pi n_f L(r_{ii}\Delta W_{m,i} - r_{ij}\Delta W_{m,j})(A/2)\cos(n_f t)}{16EW_{0,i} + 8\pi E\Delta W_{m,i} - \pi L(A/2)\sin(n_f t) + 2\pi\rho_w g D L} \tag{A8}$$

where r_{ii} corresponds to the interaction between paired tiger stripes, and r_{ij} corresponds to the interaction between the outboard slot pair and the inboard slot pair. When the deformation is in phase between paired tiger stripes, r_{ii} is in the range $0 < r_{ii} < 1$ (deformation-promoting) and r_{ij} is negative (deformation-retarding).

For the solutions that match post-2005 observations, the slots track each other within 20% of power output and within 1 hr in phase, making it hard to use stripe-to-stripe differences to test the model. However, the slot-pairs can deform very differently for parameters that may be encountered during Enceladus' geologic evolution (§A7).

Interactions between slots may be relevant to the origin of the parallel, equally-spaced tiger stripes: once a slot is established, it will produce bending stresses in the adjacent shell that favor failure at distances of about one slot width on either side. This preferred wavelength is found for icebergs on Earth [*Reeh*, 1968].

A4. Turbulent dissipation.

Extensional (compressional) stress causes h to fall (rise) which draws water into the slot from the ocean (expels water from the slot into the ocean). Velocity V depends on the pressure gradient ∇P, the roughness of the slot walls k, and the Reynolds number Re. Here $\nabla P = (D+h)^{-1}(\sigma_n(t) - 2(r_{ii}W_{m,i} - r_{ij}W_{m,j})E/L)$. Velocities normal to the crack wall are much smaller than velocities parallel to the crack wall, and we also ignore flow parallel to the long axis of the tiger stripes (which is conservative in terms of the power produced by turbulent dissipation; §A.6). Combining the Darcy-Weisbach and Colebrook-White equations gives (*Nalluri & Featherstone* [2009], their Equation 4.10):

$$|V| = -2\sqrt{2g_E d S_f}\,\log_{10}\left(\frac{k}{3.7d} + \frac{2.51\nu}{d\sqrt{2g_E d S_f}}\right) \tag{A9}$$

where g_E is Earth gravity, S_f is the dimensionless energy loss gradient, $\nu \approx 1.8 \times 10^{-6}$ m^2 s^{-1} is the kinematic viscosity of water at 0° C, and we set the equivalent pipe diameter d to be 4 times the mean slot half-width $W^*_{1/2}(t) = \frac{1}{2}\left(2W_0 + \frac{\pi}{2}\Delta W_m\right)$. The first term inside the brackets accounts for rough turbulent flow, which dominates for $|V| \sim 1$ m/s, $k >$ 0.01 m (Enceladus-relevant conditions), so

$$|Q| \approx 2LW^*_{1/2} - 2\sqrt{2g_E(4W^*_{1/2})\left|\frac{\Delta P}{\left(D - \Delta P\frac{1}{\rho_w g}\right)}\frac{1}{\rho_w g_E}\right|}\log_{10}\left(\frac{k}{14.8W^*_{1/2}}\right) \tag{A10}$$

where

$$\Delta P = \sigma_n \sin(n_f t) - (r_{ii}W_{m,i} - r_{ij}W_{m,j})2E/L \tag{A11}$$

The sign of Q (positive for inflow into the slot) is set equal to the sign of ∇P.

We now have an expression for Q which can be substituted in (Eqn. A8) to solve for $\Delta W_m(t)$. From $\Delta W_m(t)$, we next seek $F(t)$, the average power dissipated per length of tiger stripe. This could be calculated self-consistently from S_f. From *Tritton* [1988] (their Fig. 2.11), the nondimensional average pressure gradient ξ is given by the maximum of ξ_l (laminar) and ξ_t (turbulent)

$$\xi = \max(\xi_l, \xi_t)$$

$$\xi_l = 32Re$$

$$\xi_t = 0.0337Re^{\sim 1.9} \tag{A12}$$

where $Re = 2W^*_{1/2}(t)\ V(t)\ /\ \nu$. The power per unit length is then

$$F \approx |V| \frac{D\xi\nu^2}{\rho_w(2W_0 + (\pi/2)\Delta W_m)^2} \tag{A13}$$

where we neglect the difference between D and $D + h$, assume a static pressure gradient, and advect water parcels through the gradient at speed $|V|$. Most of this power will go (at steady state) into evaporative losses at the water table or into the ice, rather than into the ocean: heat flow scales as $1/\delta_{bl}$, and boundary layer thicknesses δ_{bl} are small within the slot. In addition, heated water is buoyant relative to cold water of the same salinity (for salinity > 2 %, which is likely for Enceladus) so it will underplate the slots (either as a sheet, or concentrated in cupolas beneath slots). The total power for the slot is $LF(t)$, and because the change in water temperature during one tidal cycle is $\ll$1K, the diurnal-mean F is used to compare to observations (Figs. 2-3).

Fig. S4 shows results for uncoupled slots, $W_0 = \{0.25, 0.375, 0.5, ...2.5\}$ m, $L = 100$ km, $S = Z = 35$ km.

Fig. S5 shows results for coupled slots of unequal length, $W_0 = \{0.25, 0.375, 0.5, ...2.5\}$ m, $L_{Alexandria} = L_{Damascus} = 93$ km, $L_{Baghdad} = L_{Cairo} = 151$ km, $S = Z = 35$ km.

A5. Ice inflow and melt-back

In isostatic equilibrium, a differential stress σ_x drives viscous ice inflow into the slot (Fig. S6) [*McKenzie et al.*, 2000]. σ_x reaches a maximum of $g\rho_i(Z - H)$ at the water table, where $g \approx 0.1$ m/s^2 is Enceladus gravity, and tapers linearly to zero at the moon's surface and at the ocean inlet. The corresponding strain rate, $\dot{\epsilon}_{xx}(z)$, is given by

$$\dot{\epsilon}_{xx}(z) = \frac{1}{8} N(T) \sigma_x(z)^3 \tag{A14}$$

where $N(T)$ is the effective viscosity of ice I and the factor of 1/8 assumes confinement in the along-slot (y) direction [*Cuffey & Patterson* [2010], p. 62]. Solid-ice flow is slower than the oscillating liquid-water flow in the slot. Most of the flow will occur for T>200K, $\sigma_x \sim 10^5$ Pa, and for these conditions $N(T)$ is well-constrained (these flow conditions correspond to terrestrial ice sheets). To solve for $\dot{\epsilon}_{xx}(z)$, we first calculate the ice inflow rate with a conductive geotherm:

$$T(z) = T_s + (T_m - T_s)(z/Z) \tag{A15}$$

with Enceladus surface temperature $T_s = 60$K and ice-shell base temperature $T_m = 273$K. We log-linearly interpolate $N(T)$ from Table 3.4 in *Cuffey & Patterson* [2010] and approximate the inflow rate $V_x(z)$ as the product of $\dot{\epsilon}_{xx}(z)$ and the half-width between tiger stripes, $S/2$. This gives a peak ice inflow rate of 0.3 m/yr and a mean ice inflow rate (v_x) of 0.04 m/yr. However, this is not yet a self-consistent setup. That is because such high ice inflow rates cause rapid subsidence of cold ice from above, which perturbs the geotherm, lowering $T(z)$. Following *Moore et al.* [2007] and assuming $v_z \neq v_z(z)$ (which will be justified a posteriori),

$$\lambda = \frac{\rho_i c_p v_z Z}{k_i} \tag{A16}$$

where λ is a dimensionless Péclet number, the subsidence rate $v_z = 2\ v_x$ (for $S = Z$), ice heat capacity $c_p = 2000$ J/kg/K, and ice thermal conductivity $k_i = 2.5$ W/m/K. Then

$$T = T_{surf} + (T_m - T_{surf})\frac{e^{\lambda\xi} - 1}{e^{\lambda} - 1} \tag{A17}$$

where $\xi = z/Z$. We iterate (A17)-(A19) to find the steady state: $\overline{v_x} = 1.5$ mm/yr ($Pe \sim 8$), peak $v_x = 2$ cm/yr (Fig. S7). For $Pe \sim 8$ shear heating is negligible, validating our neglect of this term a posteriori. At steady state, with these approximations, 90% of the melt-back comes from the lowermost 12% of the ice shell, which validates the approximation $v_z \neq v_z(z)$ made above. Faster ice inflow near the base of the shell will narrow the slot at its base, until local enhancement of turbulent dissipation in the liquid-water slot at the narrowed ocean inlet generates enough melt-back to balance inflow. Lateral conduction of heat from the liquid slot into the ice prism is unimportant (in the upper parts of the ice shell, the viscosity of slightly-warmed cold ice is still negligible, and once the ice is warm enough to flow it moves toward the slot so quickly that the positive feedback of conductive warming is small).

Ice lost by melting near the base of the ice shell is in balance (at steady state) with ice gained near the top of the ice shell by condensation and by frost accumulation. In a horizontal average, subsidence creates accommodation space for the near-surface build-up of condensates (an inevitable consequence of geysering, that would otherwise be expected to plug up conduits). The distribution of condensates across the ice surface depends on the poorly-understood mechanics of the uppermost kilometer of Enceladus' ice shell [*Davis et al.*, 1983; *Collins et al.*, 2009; *Barr & Preuss*, 2010; *Martens et al.*, 2015], and on the long-term average partitioning of condensates between ballistic rainout and fissure-wall condensation [*Schenk et al.*, 2011]. Because upon condensation to ice, water vapor gives up the latent heat of vaporization l_{vap}, we predict a total (four-stripe) tiger stripe terrain thermal emission of $4\ l_{vap}\, v_z\, \rho_i\, L\, S \approx 5$ GW. The observed value is (4.6 ± 0.2) GW, rising to ~ 5 GW if the latent heat represented by the vapor escaping from Enceladus is included. The data match the model.

Encouragingly, this correct prediction of the power output of Enceladus requires only S, Z, g, and a simple water ice rheology.

The rheological compilation of *Cuffey & Patterson* [2010] shows that most real ice sheets deform at rates fit by (A14) with $N(T)$ between $1\times$ and $5\times$ values inferred from laboratory experiments. Variations within this range have remarkably little effect on the Enceladus steady-state power output: 5-fold decrease in viscosity leads to only a 1.5-fold change in system mass/energy flux (6-7 GW output for Enceladus values). This buffering suggests that a more sophisticated model of the depth-dependent effective viscosity of the prism (which might include visco-elasto-plastic rheology, and 3D effects) would not greatly alter the equilibrium values found with the simple model used here.

Power is also quite insensitive to ice shell thickness (4.3 ± 0.3 GW for 20 km $< z <$ 100 km and fixed tiger stripe spacing) (Fig. S8). Within the range 20 km $< z <$ 100 km, two competing effects on equilibrium power output almost cancel. (1) Holding λ fixed, ice melt-back is faster for thicker shells because the differential stresses are larger (a more massive overburden column, with increased column-averaged gravitational acceleration), and because there is a greater absolute thickness of material at any given temperature. (2) Opposing this, holding mass/energy flux fixed, the temperature structure is colder for thicker shells because the greater vertical distances favor advection over diffusion (higher Pe for the same velocity). Effect (2) defeats effect (1) for $z > 100$ km shells, which have slightly lower power output. Effect (1) defeats effect (2) for $z < 20$ km shells, which have much lower power output (Fig. S8). Gravity-derived estimates of shell thickness (30-40 km; *Iess et al.* [2014]) correspond to the shell thickness that maximizes power output in our model.

Our results suggest that in terms of ice shell thickness, slot numbers, and slot geometry, Enceladus' current configuration is optimized for power. The system power output (for fixed system width) is not much less for long narrowly-spaced tiger stripes than for widely-spaced tiger stripes. However, narrowly-spaced slots could not be as long as the observed tiger stripes without undergoing elastic slot-slot interactions that would prevent the system from being long-lived (§A.7). The tendency for system power output to be at maximum for ice shell thickness > 30 km does not depend on the spacing between tiger stripes. Short narrowly-spaced slots would not have a large per-area power output (averaging over the tiger stripe terrain).

In steady-state geyser tectonics, unobserved melt-back contributes only $l_{melt}/(l_{vap}+l_{melt})$ = 12% of the energy demand that is balanced by viscous dissipation (where l_{melt} = 334 kJ/kg is the latent heat of fusion of water). If we are wrong and the tiger stripe terrain has not yet reached geyser-tectonic steady state, then the power demand is higher because the bulk inflow rate is greater, but within the envelope of

A6. Stability of slots.

Diurnal tidal pumping within slots helps to maintain the observed "sheet-like" configuration of Enceladus eruptions [*Spitale et al.*, 2014; *Hurley et al.*, 2015]. The observed maintenance of "sheet-like" eruptions on Enceladus is a surprise because on Earth sheet-like magmatic eruptions quickly evolve into pipe-like conduits through a positive feedback between temperature and local width. We interpret the sheet-like surface venting as simply the surface counterpart to slot-like liquid water conduits, whose geometry is maintained by along-slot stirring which evens out temperatures. Stirring is driven by along-slot gradients in the amplitude of the tidally-driven diurnal cycles in slot width, flow velocity, and turbulent dissipation, which have peak amplitude near the middle of the slot for simple slot geometries. (We have carried out sensitivity tests using the full, branched geometry of the tiger stripes and verified that this expectation from simple slots holds for realistic tiger stripe geometry). These gradients from the center to the ends of each slot, together with minor along-slot tidal phase variations (Fig. S2), drive bulk along-slot flows with velocity $O(10\%)$ that of the vertical flow. (The contribution of this flow to heat production within the slot is neglected in our averaged equations (A10)-(A13), which is conservative in terms of calculating the importance of turbulent dissipation). Because flow within the slot is turbulent, the along-slot bulk flow is stirred into boundary layers adjacent to the ice during each tidal cycle, leading to an effective stirring timescale of $O(10\%) L/\overline{V} \sim 40$ days. Currents in the ocean (which have been calculated at u >1 cm/s for Europa; *Soderlund et al.* [2014]) will sweep warm water along the base of the slot during the compressive phase of the cycle prior to re-ingestion during the tensile phase of the cycle, and this will help to equalize temperatures within the crack on a timescale L_{ts}/u ($\sim$ 100 days for u = 1 cm/s).

These stirring timescales are short compared to the timescales for slot-widening via inflow and melt-back, and this helps to explain why the tiger stripes do not suffer end freezing nor undergo a corrugation instability. An upper bound on melt-back speed comes from complete dissipation of the tidal stress cycle in the water, for which power per unit volume is A/p. If the latent heat of melting is 334 MJ/m^3, then the timescale for melt-back doubling of the width of an initially 1m-wide slot is not less than 5000 days. Viscous inflow of wall ice is also slow, which will be shown later. This ratio of timescales favors suppression of the fissure-to-pipe transition. This contrasts with magmatic fissures on Earth, for which along-slot thermal homogenization timescales are long compared to freeze-out timescales, so that pipes develop. Although a full treatment of instabilities in melt-back will require detailed modeling that so far has not been attempted even for Earth (state-of-the-art models use highly idealized heating parameters [*Dallaston & Hewitt*, 2014]), this heuristic argument suggests that long-lived slots may be at the root of the observed longevity of fissure eruptions on Enceladus. This mechanism can be tested through the prediction that the long-term average power output from should not be strongly variable along slot, in contrast to crack models (e.g. *Smith-Konter & Pappalardo* [2008]; *Nimmo et al.* [2007]; *Hurford et al.* [2009] which predict strongly varying power generation along wiggles in the tiger stripes.

This argument for slot stability conservatively ignores ice-bridge disruption by strike-slip motion (O(1 m) per cycle; *Smith-Konter & Pappalardo* [2008]), which could arrest the conversion of slots to pipes. If pipes do form, they should be short-lived: pipes do not change their cross-sectional area much during a tidal cycle, so unless the ocean's pressure undergoes a high-amplitude diurnal pressure cycle, turbulent dissipation of diurnal flow within pipes will be minor. Short-lived pipes may correspond to jets that appear in *Cassini* images [*Spitale & Porco*, 2007]; alternatives include artifacts of viewing geometry [*Spitale et al.*, 2014], along-slot variations in the width of fractures about the water table, or some combination.

We have treated the ocean as a constant-pressure bath and ignored feedbacks of flushed water on ocean pressure, which could be significant.

Fig. 2 in the main text shows how $W_0 \sim 1$ m can be stable to changes in mean width: on the branch where increases in W_0 reduce power output, melt-back is a negative feedback on melt rate.

The thermal emission, if conductive, averages over 10^3 yr timescales because the conductive path length from the fissure walls to the center of the thermal-emission belts is hundreds of meters. Thus, the fact that thermal emission from the four tiger stripes is comparable indicates that the spacecraft-era continuity of activity from all four stripes is representative of activity on 10^3 yr timescales. The fact that the emission is of the same order of magnitude further suggests a regulating mechanism maintaining the stripes at that power, and slot stabilization by turbulent dissipation is one such regulating mechanism (Fig. 2).

A6.1. Top freezing.

At steady state, the latent heat of vapor escaping the water table must be balanced by heat supplied from the water. Vertical resupply is assisted by exsolving, ascending bubbles. The km-scale changes in h help: some of the vapor is supplied from ice that is warmed during the time that it is underwater, rather than directly from the water. The changes in water level and in slot width also help to break up any ice that does form.

A7. Sensitivity tests and extensions.

F scales as σ_n^2, and σ_n increases with h_2 and l_2; these Love numbers are in turn sensitive to Enceladus' internal structure [*Olgin et al.*, 2011]. If the ocean is locally grounded, that should not greatly change the tidal distortion. However, if there is only a regional sea, that would make a big difference, reducing h_2 and thus the magnitude of turbulent dissipation.

Change E (results are tedious)

$Q = \{0.1,0\}$ (inhibited communication ... rather trivial result.)

We find $F \propto L^{\sim 2}$ for variations in the length of slots that do not interact elastically. Sheets of emission appear most concentrated from the central-most 100 km of the tiger stripes, and it is possible that this represents the currently-active section of the stripes: this possibility is shown in Fig. 2 and Fig. S10.

Next we consider variations in the length of paired slots that interact elastically. Here again $F \propto L^{\sim 2}$ is expected, but nonlinear effects become important. Consider two slots (or two pairs of slots) i and j whose edges are subject to time-varying internal pressure and which interact through elastic stresses. The equations of motion on diurnal timescales can be written as:

$$\frac{\partial \Delta W_{m,i}}{\partial t} \sim Q_i + k_1 F(t) + k_2 F(t)(r_{ii}\Delta W_{m,i} - r_{ji}\Delta W_{m,j})$$
$$\frac{\partial \Delta W_{m,j}}{\partial t} \sim Q_j + k_3 G(t) + k_4 G(t)(r_{jj}\Delta W_{m,j} - r_{ij}\Delta W_{m,i}) \tag{A18}$$

and the matrix of coupling coefficients is

$$\begin{pmatrix} r_{ii} & -r_{ij} \\ -r_{ji} & r_{jj} \end{pmatrix}$$

where the r terms are calculated using the output of a boundary-element code (§A.3). For slots of the observed length of Enceladus' tiger stripes (Fig. 2), the solution is stable, although the power is reduced relative to the case where slots of the same length are not elastically coupled (Fig. 2, Fig. S4, Fig. S5). For sufficiently extended or close-spaced parallel slots the determinant of the coupling matrix becomes negative, and the coupled equations define a saddle-node instability. In our model, this instability manifests as water piracy on diurnal timescales: one slot swells, with large-amplitude oscillations, and the other loses almost all its water and undergoes small-amplitude oscillations. Water piracy's long-term consequence would be that the pirated slot would become inactive due to reduced turbulent dissipation. This immediately suggests a mechanism for limiting the size both of Enceladus' tiger stripe terrain and of the three fossilized tectonized regions of Miranda (Uranus V), which taken together have angular diameters $(70\pm10)^\circ$, $n = 4$. Slots beyond a certain length would suffer destructive interference (if we suppose that the spacing of slots is set by the thickness of the ice shell). Salts on the surface of Europa (Jupiter II) suggest that cryo-volcanic conduits link Europa's surface to its sub-ice ocean [*Brown & Hand*, 2013], and if long water-filled slots on Europa destructively interfered, then this would affect the sustainability of activity [*Roth et al.*, 2014].

A8. Insufficiency of non-tidal power sources and links to very long timescales.

Our model assumes that tidal heating powers Enceladus [*Nimmo & Spencer*, 2013; *McKinnon*, 2013; *Travis & Schubert*, 2015], so we briefly review the insufficiency of non-tidal heating sources. Joule heating [*Hand et al.*, 2011] is not important for Enceladus. Exothermic water-rock interactions could contribute to observed thermal emission at the 10% level [*Malamud & Prialnik*, 2013]. Tidal dissipation in porous seafloor sediment is negligible for Enceladus [*Vance et al.*, 2007]. Radiogenic heating is <0.32 GW assuming a chondritic composition for Enceladus' rock core [*Porco et al.*, 2006].

On timescales much longer than the tectonic-resurfacing age of the South Polar terrain (<10^6 yr, from crater counts), orbital dynamics require that at least one of the following are true [*Meyer & Wisdom*, 2007]: (1) Enceladus' surface power output is intermittent; (2) the tidal dissipation quality factor of Saturn is less than assumed, and the mid-sized icy satellites of Saturn are much younger than 4.5 Gyr [*Charnoz et al.*, 2007].

Our work does not address this Gyr-timescale, "deep" problem of sustaining Enceladus' ocean-fuelled eruptions. We have focused instead on the "shallow" problem of how the ice shell tectonics, liquid water plumbing system, and eruptions are interrelated at timescales from the 10^1 yr observational baseline up to the tiger-stripe terrain's tectonic refresh timescale for the ($4LSZ\rho_i l_{vap}/5\mathrm{GW} \approx 10^7 yr$). Beyond the tectonic refresh time geologic information is lost, although terrains far from the tiger stripes [*Bland et al.*, 2012] may record Enceladus' activity at earlier times. At these earlier times, orbital parameters are unpredictable, the ocean may freeze or become unbound from the rock core, and any regional ocean may slide sideways, shoulder ice aside, and globalize.

Of the subset of geyser water that goes into orbit around Saturn, very little returns to the tiger stripe terrain. Therefore, if strict steady state in the ice shell is to be maintained, mass escaping from Enceladus should be balanced by mass supplied by the ocean. Tracking changes in ocean volume over millions of years is beyond the scope of this study, but the worst-case imbalance – supposing that water escaping from Enceladus is entirely sourced from the ice shell, with zero replacement – is only $\sim$10% (200 kg/s escapes, 1800 kg/s circulates).

Author contributions

E.S.K. conceived research, E.S.K. and A.M.R. designed research, and E.S.K. carried out research. A.M.R. wrote the boundary element code. Both authors contributed to the interpretation of the results.

Notes

1. Enceladus-sourced snowdrifts on small moons neighboring Enceladus can be >10 m thick, indicating $\gg 10^3$ yr deposition, with the exact number depending on unmodeled details of ice-grain orbital dynamics [*Hirata et al.*, 2014].
2. For outflow velocities of 300-500 m/s, and near-surface vent temperatures of $\sim$200K [*Goguen et al.*, 2013], the effective mean fracture width implied by UV occultation constraints on vapor flux is only $\sim$1 mm.
3. This can be seen by considering an inviscid fluid column sealed at the bottom and subject instantaneously to a pressure gradient of $P_{max}/H(t=0) \approx P_{max}$ / $0.9Z$. The column adjusts to $H(t=\tau_{adj}) = P_{max}/(\rho_w g)$ where τ_{adj} is an adjustment timescale. Euler's equation of inviscid motion gives $H(t) \sim (P_{max}/\rho_w H)t^2$, so $\tau_{adj} \sim \sqrt{H/g}$. The water table tracks the rising pressure when $\tau_{adj}/p \ll 1$. For $Z \sim 20$ km and $P_{max} = 1$ bar, this ratio of timescales is $O(10^{-3})$ for Enceladus and $O(10^{-4})$ for Europa.
4. Sublimation cooling cannot be balanced by convection (e.g., [*Postberg et al.*, 2009]). If sublimation cooling is balanced by latent heat of water flowing from the ocean, then $\sim$10 volumes of water must freeze to power the sublimation of 1 volume of water. Again this leads to rapid freezing for reasonable crack volumes.

References

Abramov, O., & Spencer, J.R. (2009), Endogenic heat from Enceladus' south polar fractures: New observations, and models of conductive surface heating, *Icarus*, *199*, 189-196.

Archinal, B. A., et al. (2011), Report of the IAU Working Group on Cartographic Coordinates and Rotational Elements: 2009, *Celestial Mechanics and Dynamical Astronomy*, *109*, 101-135.

Barr, Amy C.; Preuss, Lauren J. (2010), On the origin of south polar folds on Enceladus, *Icarus*, *208*, 499-503.

Bland, M.T., et al. (2012), Enceladus' extreme heat flux as revealed by its relaxed craters *Geophys. Res. Lett.*, *39*, L17204.

Běhounková, Marie; Tobie, Gabriel; Choblet, Gaël; Čadek, Ondřej, Tidally-induced melting events as the origin of south-pole activity on Enceladus, *Icarus*, *219*, 655-664.

Brown, M.E., & Hand, K.P. (2013), Salts and radiation products on the surface of Europa, *Astron. J.*, *145*, 110.

Bruce, P.M., & Huppert, H.E. (1989), Thermal control of basaltic fissure eruptions, *Nature*, *342*, 665-667.

Charnoz, S., Salmon., J., & Crida., A. (2007), The recent formation of Saturn's moonlets from viscous spreading of the main rings, *Nature*, *465*, 752-754.

Chen, E. M. A.; Nimmo, F.; Glatzmaier, G. A. (2014), Tidal heating in icy satellite oceans, *Icarus*, *229*, 11-30

Collins, Geoffrey C., et al. (2009), Tectonics of the outer planet satellites, pp. 264-350 *in* Watters, T.R., & Schultz, R.A. (Eds). *Planetary Tectonics*, Cambridge University Press.

Crawford, G. D.; Stevenson, D. J. (1983), Gas-driven water volcanism in the resurfacing of Europa, *Icarus*, *73*, 66-79, DOI:10.1016/0019-1035(88)90085-1

Crouch, S.L., & Starfield, A.M. (1983), Boundary element methods in solid mecchanics, George Allen & Unwin.

Cuffey, K., & Patterson, W. (2010), The physics of glaciers, 4th edition, Academic Press.

Davis, D., Suppe, J., & Dahlen, F.A. (1983), Mechanics of fold-and-thrust belts and accretionary wedges, *J. Geophys. Res.*, *88*, 1153-1172.

Dallaston, M.C., and I.J. Hewitt (2014), Free-boundary models of a meltwater conduit, *Physics of Fluids*, *26*, 083101.

Dong, Y.; Hill, T. W.; Teolis, B. D.; Magee, B. A.; Waite, J. H. (2011), The water vapor plumes of Enceladus, *Journal of Geophysical Research: Space Physics*, *116*, A10204.

Gaidos, Eric J.; Nimmo, Francis (2000), Planetary science: Tectonics and water on Europa, *Nature*, *405*, 637 (2000).

Goguen et al. (2013), The temperature and width of an active fissure on Enceladus measured with Cassini VIMS during the 14 April 2012 South Pole flyover, *Icarus*, *226*, 1128-1137.

Gudmundsson, Agust (2011), Rock fractures in geological processes, Cambridge University Press, 592 pp.

Hansen, C. J.; Shemansky, D. E.; Esposito, L. W.; Stewart, A. I. F.; Lewis, B. R.; Colwell, J. E.; Hendrix, A. R.; West, R. A.; Waite, J. H., Jr.; Teolis, B.; Magee, B. A., The composition and structure of the Enceladus plume, *Geophysical Research Letters*, *38*, L11202.

Hand, K. P.; Khurana, K. K.; Chyba, C. F. (2011), Joule heating of the south polar terrain on Enceladus, *Journal of Geophysical Research*, *116*, E4, E04010.

Hedman, M. M., et al. (2013), An observed correlation between plume activity and tidal stresses on Enceladus, *Nature*, *500*, 182-184.

Hirata, Naoyuki; Miyamoto, Hideaki; Showman, Adam P. (2014), Particle deposition on the saturnian satellites from ephemeral cryovolcanism on Enceladus, *Geophysical Research Letters*, *41*, 4135-4141.

Hsu, Hsiang-Wen, et al. (2013), Silica nanoparticles as an evidence of hydrothermal activities at Enceladus, *American Astronomical Society, DPS meeting* #45, #416.04

Hurford, T. A., et al. (2009), Geological implications of a physical libration on Enceladus, *Icarus*, *203*, 541-552.

Hurley, D.M., et al. (2015), Properties of the vapor release from Enceladus' tiger stripes from modeling and Cassini INMS data, *46th Lunar and Planetary Science Conference*, Houston, Texas, abstract no. 2318.

Ingersoll, Andrew P.; Pankine, Alexey A. (2010), Subsurface heat transfer on Enceladus: Conditions under which melting occurs, *Icarus*, *206*, 594-607.

Iess, L., et al. (2014), The gravity field and interior structure of Enceladus, *Science*, *344*, 78-80.

Jia, Y.-D., et al., Interaction of Saturn's magnetosphere and its moons: 3. Time variation of the Enceladus plume, *Journal of Geophysical Research: Space Physics*, *115*, A12243.

Malamud, Uri; Prialnik, Dina (2013), Modeling serpentinization: Applied to the early evolution of Enceladus and Mimas, *Icarus*, *225*, 763-774.

Martens, H., Ingersoll., A.P., Ewald., S.P., Helfenstein, P., & Giese, B. (2015), Spatial distribution of ice blocks on Enceladus and implications for their origin and emplacement, *Icarus*, *245*, 162-176.

Matson, Dennis L., et al. (2012), Enceladus: A hypothesis for bringing both heat and chemicals to the surface, *Icarus*, *221*, 53-62.

McKay, Christopher P.; Anbar, Ariel D.; Porco, Carolyn; Tsou, Peter (2014), Follow the Plume: The Habitability of Enceladus, *Astrobiology*, *14*, 352-355.

McKenzie, D., et al., Characteristics and consequences of flow in the lower crust, *J. Geophys. Res. - Solid Earth*, *105*, 11029-11046.

McKinnon, W.B. (2013), The shape of Enceladus as explained by an irregular core: Implications for gravity, libration, and survival of its subsurface ocean, *J. Geophys. Res.*, *118*, 1775-1788.

Meyer, Jennifer; Wisdom, Jack (2007), Tidal heating in Enceladus, *Icarus*, *188*, 535-539.

Mitchell, Karl (2005), Coupled conduit flow and shape in explosive volcanic eruptions, *J. Volcanol. Geotherm. Res.*, *143*, 187-203.

Moore, W.B., et al. (2007), The interior of Io, *in* Io after *Galileo*, edited by Rosaly M.C. Lopes and John C. Spencer, Springer-Praxis Books.

Murray, Carl D., & Dermott, Stanley F. (2000), Solar System Dynamics, Cambridge University Press, 608 pp.

Nakajima, Miki; Ingersoll, A. P. (2012), Enceladus Plumes: A Boiling Liquid Model, *American Astronomical Society, DPS meeting* #44, #112.04

Nalluri & Featherstone's Civil Engineering Hydraulics, 5th edition, revised by M. Marriott. Wiley-Blackwell.

Nimmo, Francis (2004), What is the Young's modulus of ice?, *Conference on Europa's Icy Shell*, abstract #7005.

Nimmo, Francis and Manga, Michael (2009), Geodynamics of Europa's ice shell, in Pappalardo, R.T., McKinnon, W.B., and Khurana, K., eds., *Europa*, University of Arizona Press, p. 382-404.

Spencer, John R.; Nimmo, Francis (2013), Enceladus: An Active Ice World in the Saturn System, *Annual Review of Earth and Planetary Sciences*, *41*, 693-717.

Nimmo, Francis, et al. (2007), Shear heating as the origin of the plumes and heat flux on Enceladus, *Nature*, *447*, 288-291.

Nimmo, Francis, et al. (2014), Tidally modulated eruptions on Enceladus: *Cassini* observations and models, *Astronomical J.*, *148*, 48.

Olgin, J.G., Smith-Konter, B.R., & Pappalardo, R.T. (2011), Limits of Enceladus's ice shell thickness from tidally driven tiger stripe failure, *Geophys. Res. Lett.*, *38*, L02201.

Parkinson, Christopher D.; Liang, Mao-Chang; Yung, Yuk L.; Kirschivnk, Joseph L. (2008), Habitability of Enceladus: Planetary Conditions for Life, *Origins of Life and Evolution of Biospheres*, *38*, 355-369.

Petigura, Erik A.; Marcy, Geoffrey W.; Howard, Andrew W. (2013), A Plateau in the Planet Population below Twice the Size of Earth, *Astrophysical Journal*, *770*, article id. 69.

Porco, C.; DiNino, D.; Nimmo, F. (2013), How the Jets, Heat and Tidal Stresses Across the South Polar Terrain of Enceladus are Related, *Astronomical J.*, *148*, 45.

Porco, C., et al. (2006), Cassini Observes the Active South Pole of Enceladus, *Science*, *311*, 1393-1401.

Postberg, F., et al. (2009), Sodium salts in E-ring ice grains from an ocean below the surface of Enceladus, *Nature*, *459*, 1098-1101.

Postberg, F., et al., (2011), A salt-water reservoir as the source of a compositionally stratified plume on Enceladus, *Nature*, *474*, 620-622.

Reeh, N. (1968), On the calving of ice from floating glaciers and ice shelves, *J. Glaciol.*, *7*, 215-232.

Roth, L., et al., (2014), Orbital epicenter is not a sufficient condition for HST/STIS detection of Europa's water vapor aurora, *Proceedings of the National Academy of Sciences*, doi:10.1073/pnas.1416671111.

Röthlisberger, Hans (1972), Water pressure in intra- and subglacial channels, *Journal of Glaciology*, *11*, 177-203.

Rubin, A.M., & Pollard, D.P. (1988), Dike-induced faulting in rift zones of Iceland and Afar, *Geology*, *16*, 413-.

Rudolph, Maxwell L., and Manga, Michael (2009), Fracture penetration in planetary ice shells, *Icarus*, *199*, 536-541.

Schmidt, Jürgen; Brilliantov, Nikolai; Spahn, Frank; Kempf, Sascha (2008), Slow dust in Enceladus' plume from condensation and wall collisions in tiger stripe fractures, *Nature*, *451*, 685-688.

Schmidt, P., Schmidt, J., & White, O. (2011), The snows of Enceladus, *EPSC-DPS Joint Meeting, Nantes, France*, *451*, 685-688.

Schulson, Erland M.; Fortt, Andrew L. (2012), Friction of ice on ice, *Journal of Geophysical Research: Solid Earth*, *117*, CiteID B12204.

Smith-Konter, Bridget; Pappalardo, Robert T. (2008), Tidally driven stress accumulation and shear failure of Enceladus's tiger stripes, *Icarus*, *198*, 435-451.

Soderlund, K.M., Schmidt, B.E., Wicht, J., & Blankenship, D.D. (2014), Ocean-driven heating of Europa's icy shell at low latitudes, *Nature Geoscience*, *7*, 16-19.

Spencer, J. R., et al. (2013), Enceladus Heat Flow from High Spatial Resolution Thermal Emission Observations *European Planetary Science Congress 2013*. Online at: http://meetings.copernicus.org/epsc2013, id.EPSC2013-840.

Spitale, Joseph N.; Porco, Carolyn C. (2007), *Nature*, *449*, 695-697.

Spitale, Joseph N.; Hurford, Terry A.; Rhoden, Alyssa R.; Berkson, Emily E.; Platts, Symeon S., Curtains for Enceladus, American Astronomical Society, DPS meeting #46, #405.01.

Stevenson, D. J. (2000), Limits on the Variation of Thickness of Europa's Ice Shell, *31st Lunar and Planetary Science Conference, March 13-17, 2000*, Houston, Texas, abstract no. 1506.

Tobie, G., Čadek, O., & Sotin, C. (2008), Solid tidal friction above a liquid water reservoir as the origin of the south polar hotspot on Enceladus, *Icarus*, *196*, 642-652.

Travis, B.J., & Schubert, G. (2015), Keeping Enceladus warm, *Icarus*, *250*, 32-42.

Tritton, D.J. (1988), Physical Fluid Dynamics, 2nd Edition, Oxford University Press.

Tsou, Peter, et al. (2012), LIFE: Life Investigation For Enceladus, A Sample Return Mission Concept in Search for Evidence of Life, *Astrobiology*, *12*, 730-742

Tyler, R. (2011), Tidal dynamical considerations constrain the state of an ocean on Enceladus, *Icarus*, *211*, 770-779.

Valko, Peter, and Michael J. Economides (1995), Hydraulic fracture mechanics, Wiley.

Vance, Steve, et al. (2007), Hydrothermal Systems in Small Ocean Planets, *Astrobiology*, *7*, 987-1005.

Wahr, John, et al. (2009), Modeling stresses on satellites due to nonsynchronous rotation and orbital eccentricity using gravitational potential theory, *Icarus*, *200*, 188-206.

Waite, J. H., Jr.; Lewis, W. S.; Magee, B. A.; Lunine, J. I.; McKinnon, W. B.; Glein, C. R.; Mousis, O.; Young, D. T.; Brockwell, T.; Westlake, J.; Nguyen, M.-J.; Teolis, B. D.; Niemann, H. B.; McNutt, R. L.; Perry, M.; Ip, W.-H., (2009), Liquid water on Enceladus from observations of ammonia and ^{40}Ar in the plume, *Nature*, *460*, 487-490.

Wylie, J.J. et al. (1999), Flow localization in fissure eruptions, *Bull. Volcanol.*, 60, 432-440.

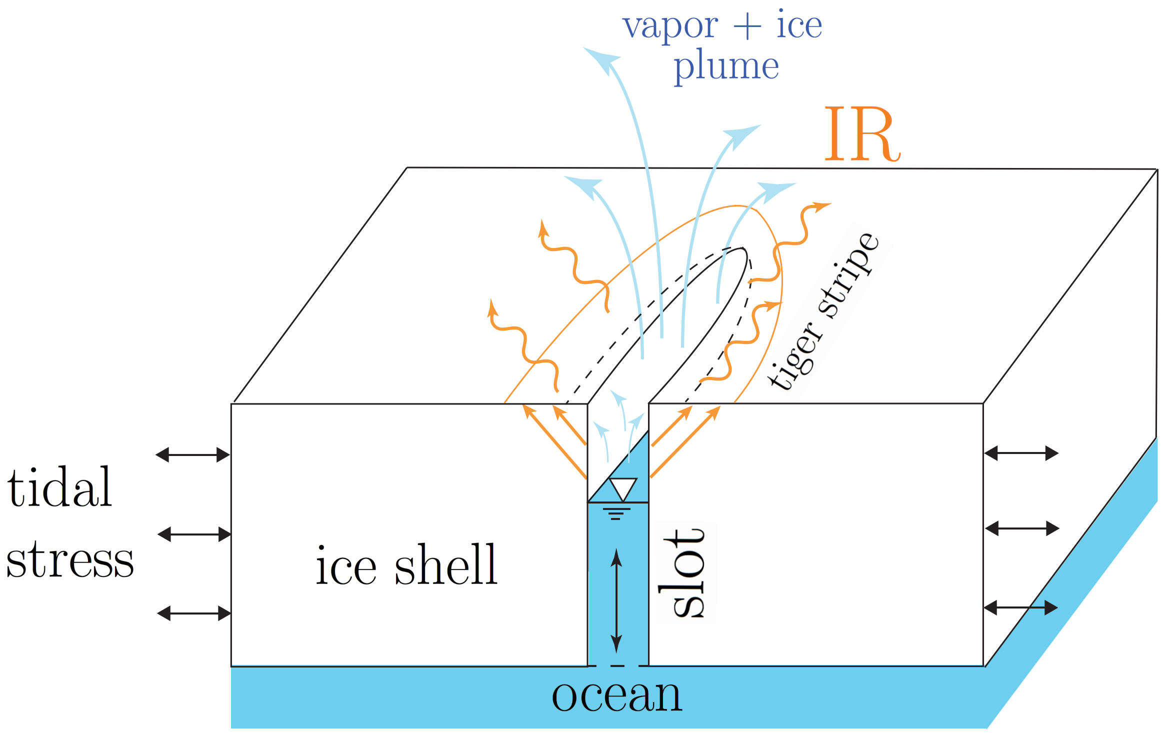

Figure 1. The geyser flux from Enceladus (blue arrows) varies on diurnal timescales, which we attribute to daily flexing (dashed lines) of the geyser source fissures by Saturn tidal stresses (horizontal arrows). Such flexing would also drive vertical flow in slots underneath the source fissures (vertical black arrow), which through viscous dissipation generates heat. This heat maintains the slots against freeze-out despite strong evaporitic cooling by vapor escaping from the water table (downward-pointing triangle), which ultimately provides heat (via condensation) for the envelope of warm surface material bracketing the tiger stripes (orange arrows).

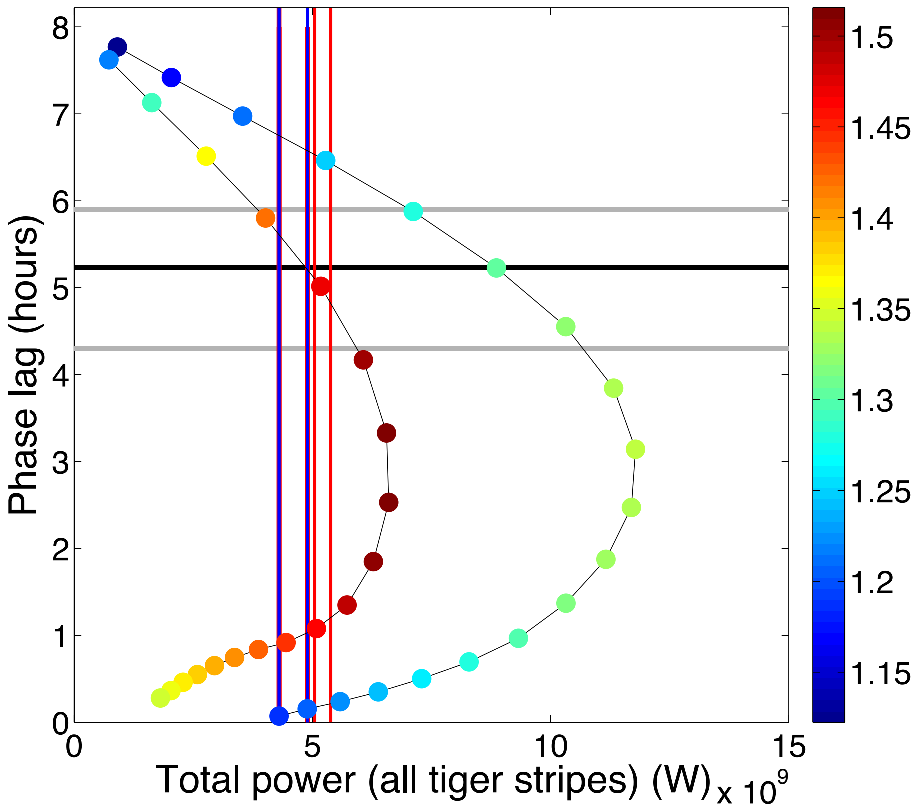

Figure 2. The turbulent dissipation that matches the observed phase lag of Enceladus (thick black horizontal line shows phase lag relative to a fiducial model, gray lines show 1σ error in observed phase lag) also matches the observed power output of Enceladus (blue vertical lines; red lines include the additional power required for vaporization of gas escaping Enceladus). The thin black curves show the mean power for (left curve) four slots of equal length 100 km, and (right curve) 93 km length outboard slots and 151 km length inboard slots. Dot color corresponds to the fractional change in aperture during the tidal cycle. For each black curve, half-width is sampled at 0.25 m width (uppermost dots) and then at 0.125 m intervals up to 2.5 m (lowermost dots). Best fit slot half-widths are 0.625-1 m.

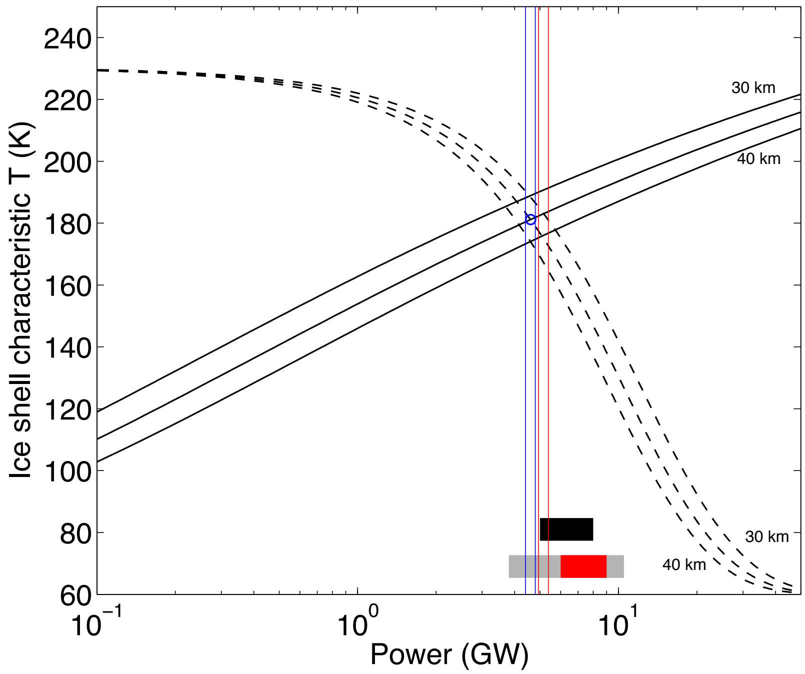

Figure 3. The power output and mass flux of Enceladus, linking 10^{-2} yr through 10^6 yr timescales. Solid black lines show the power corresponding to vaporization of the ice flowing from the ice shell into base of the slots for ice shell thicknesses of (from top) 30 km, 35 km, and 40 km (the range matching gravity data; *Iess et al.* [2014]). Dashed lines show the cooling of the ice shell corresponding to subsidence of cold ice at that mass flux; where the dashed lines intersect the solid lines, shell equilibrium is possible on Myr timescales (blue circle). The red and gray bars show the power output for the turbulent dissipation models that match the observed phase lag of Enceladus' eruptions to within 1σ and 2σ, respectively. The black bar shows the range of turbulent dissipation model runs where slot aperture varies by >1.5, consistent with the observation of large-amplitude diurnal variations in the volcanic plume. The million-year and diurnal-average power outputs implied by long-lived slots are both in agreement with the observed power output of Enceladus (blue vertical lines for tiger stripe excess IR, red including the additional energy represented by the latent heat of water vapor escaping the moon).

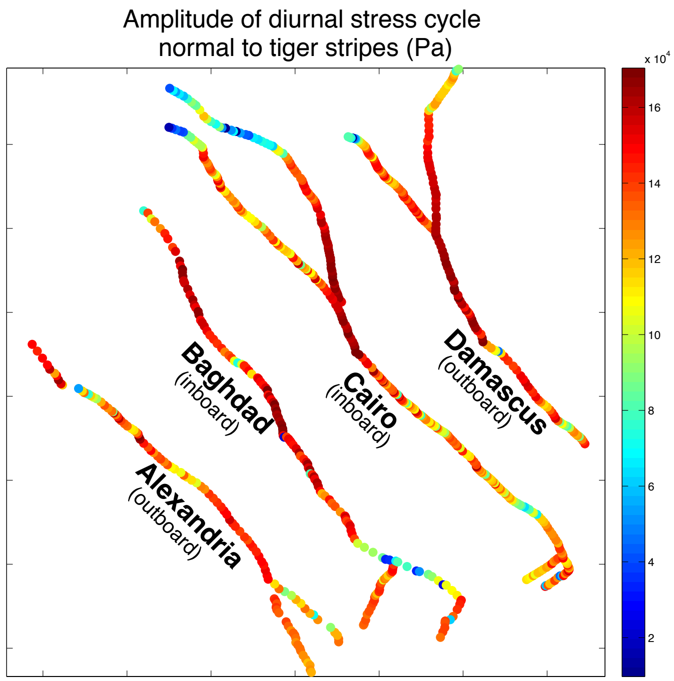

Figure S1. Map of the peak-to-trough amplitude of the diurnal cycle in normal-stress across the tiger stripes for $h_2 = 0.2$, $l_2 = 0.04$. Along-fissure lengths for tiger stripes range (in our mapping) from 133 km (Alexandria *and* Damascus) to 194 km (Cairo), mean 158 km. Great-circle distances between the tips of currently active regions [*Porco et al.*, 2014] range from 79 km (Alexandria) to 165 km (Baghdad), mean 122 km.

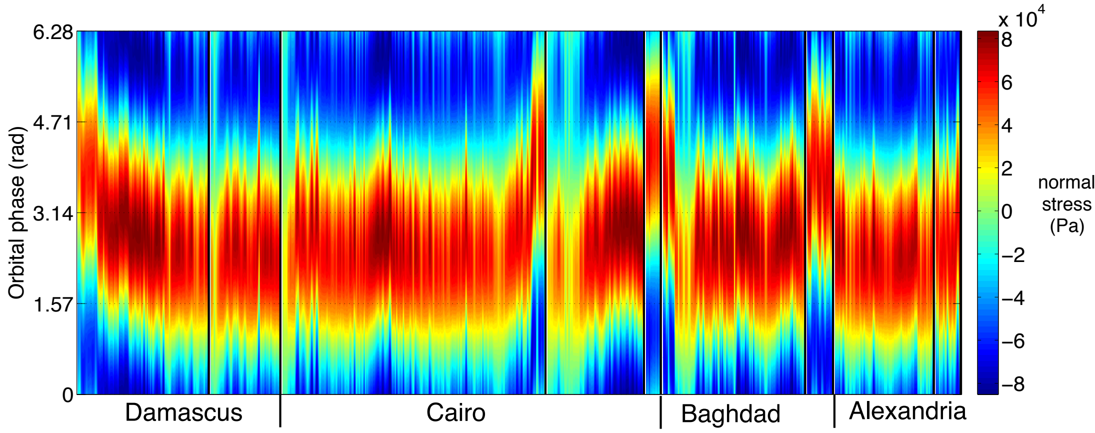

Figure S2. Contour plot of tiger stripe normal stresses as a function of phase and relative distance along the tiger stripes for $h_2 = 0.2$, $l_2 = 0.04$. Each vertical line corresponds to a single vertex picked on the tiger stripes.

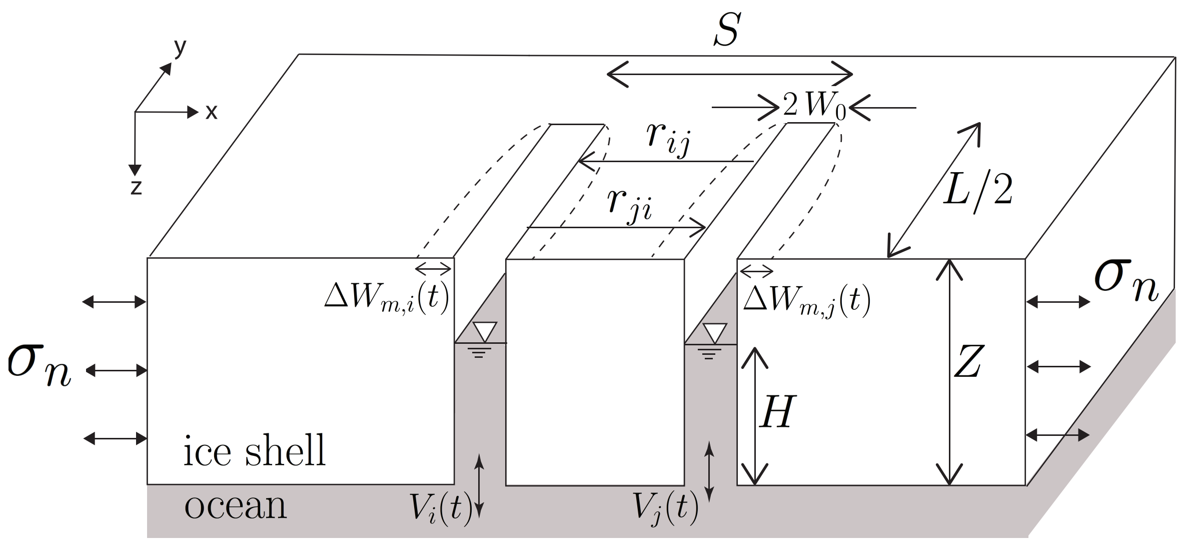

Figure S3. Definitions of terms used in model description (§A.2 - §A.3). Two parallel rectangular slots of uniform stress-free half-width W_0, length L, and spacing S, subject to tidal stress $\sigma_n(t)$, interact via elastic interaction coefficients r_{ij} and r_{ji}, leading to cycles in maximum width change $\Delta W_m(t)$. Cycles in water table height relative to zero-stress water table height H are small relative to H. Tidal flexing is coupled to water ingestion/egestion at velocity $V(t)$.

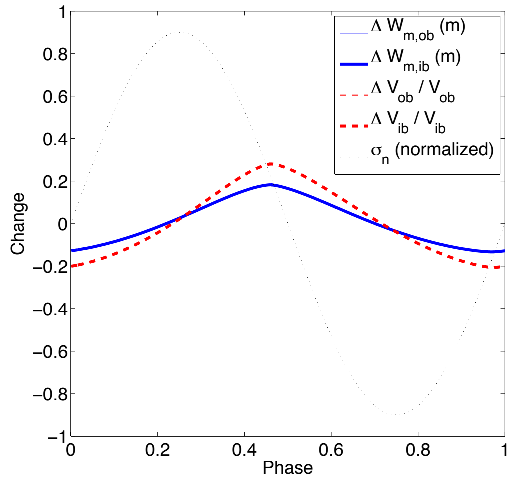
Δ W_m,ob (m)
Δ W_m,ib (m)
Δ V_ob / V_ob
Δ V_ib / V_ib
σ_n (normalized)
Change
Phase
1
0.8
0.6
0.4
0.2
0
−0.2
−0.4
−0.6
−0.8
−1
0
0.2
0.4
0.6
0.8
1

a)

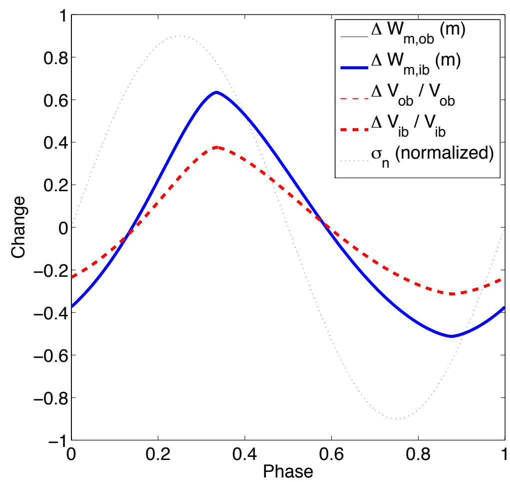
Δ W_m,ob (m)
Δ W_m,ib (m)
Δ V_ob / V_ob
Δ V_ib / V_ib
σ_n (normalized)
Change
Phase
1
0.8
0.6
0.4
0.2
0
−0.2
−0.4
−0.6
−0.8
−1
0
0.2
0.4
0.6
0.8
1

b)

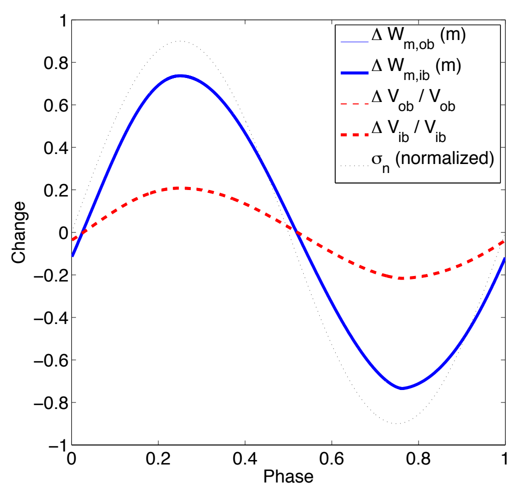
Δ W_m,ob (m)
Δ W_m,ib (m)
Δ V_ob / V_ob
Δ V_ib / V_ib
σ_n (normalized)
Change
Phase
1
0.8
0.6
0.4
0.2
0
−0.2
−0.4
−0.6
−0.8
−1
0
0.2
0.4
0.6
0.8
1

c)

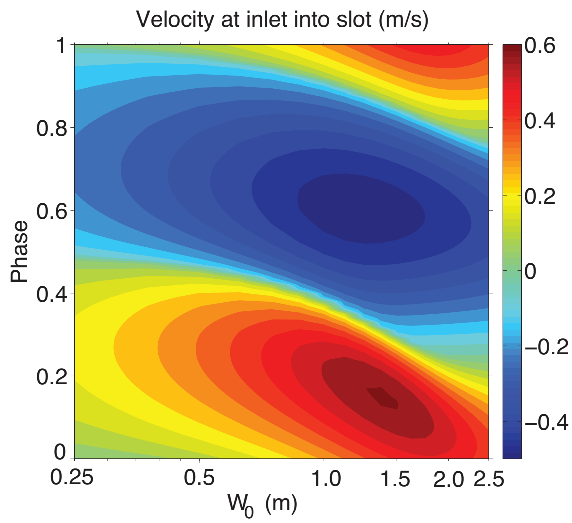

d)

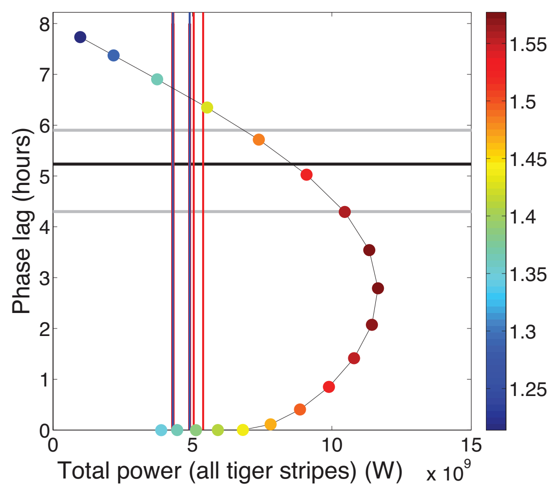

e)

Figure S4. Tidal flexing cycle for slots that do not interact elastically (for 4 slots each with L = 130 km, E = 6 GPa). (a) W_0 = 0.5 m slot. (b) W_0 = 1.25 m. (c) W_0 = 2.5 m. (d) Velocity into slot versus phase and initial width. Contour interval 0.05 m/s. (e) Phase lag versus total power output. Half-width is sampled at 0.25 m width (uppermost dots) and then at 0.125 m intervals up to 2.5 m (lowermost dots). Dot color corresponds to the fractional change in aperture during the tidal cycle. Thick black horizontal line shows phase lag relative to a fiducial model, gray lines show 1σ error in observed phase lag. Blue vertical lines show the observed power output of Enceladus; red lines include the additional power required for vaporization of gas escaping Enceladus.

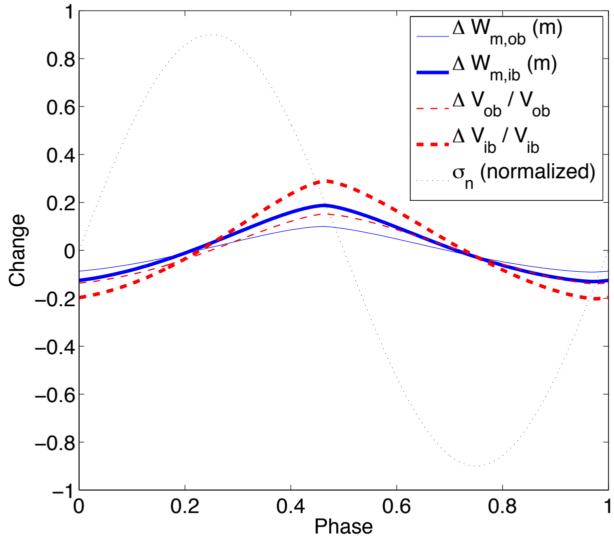
Δ W m,ob (m)
Δ W m,ib (m)
Δ V ob / V ob
Δ V ib / V ib
σ n (normalized)
Change
Phase

a)

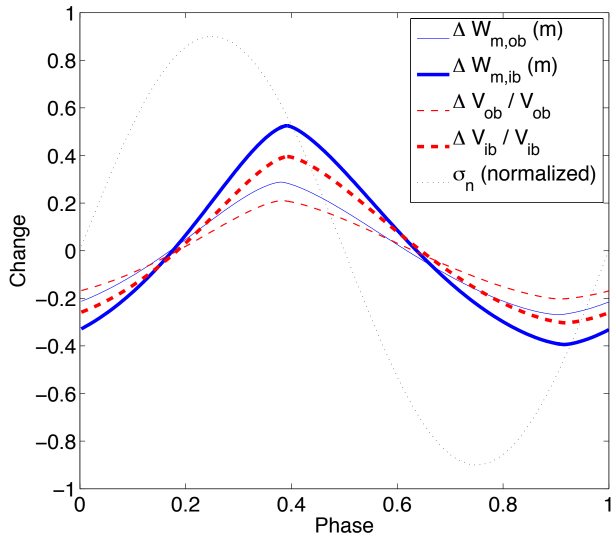
Δ W m,ob (m)
Δ W m,ib (m)
Δ V ob / V ob
Δ V ib / V ib
σ n (normalized)
Change
Phase

b)

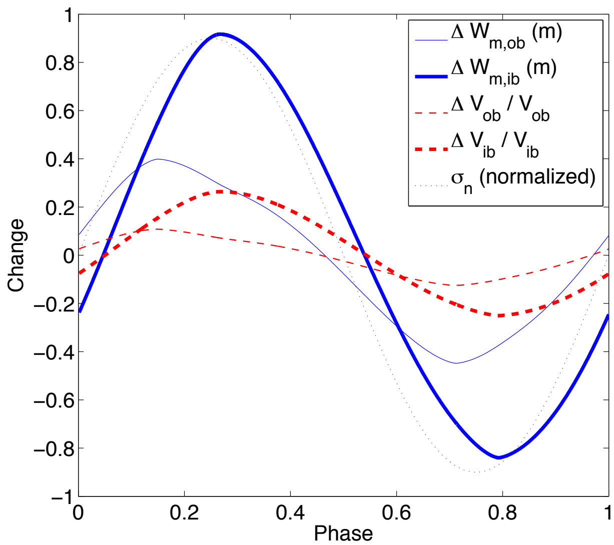
Δ W m,ob (m)
Δ W m,ib (m)
Δ V ob / V ob
Δ V ib / V ib
σ n (normalized)
Change
Phase

c)

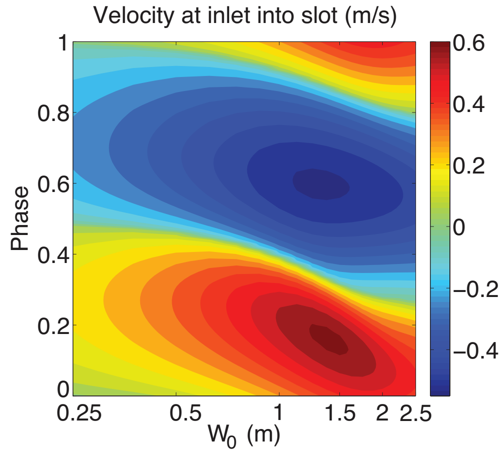

d)

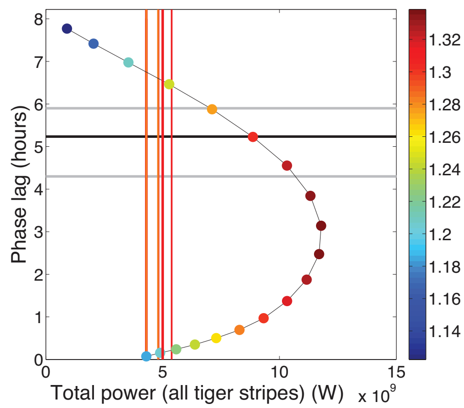

e)

Figure S5. Tidal flexing cycle for interacting slots assuming 2 inboard (*ib*) and 2 outboard (*ob*) slots, E = 6 GPa, L = 130 km. (a) $W_0 = 0.25$ m slot. (b) $W_0 = 1$ m. (c) $W_0 = 2.5$ m. Although the outboard slot leads the forcing, overall power still lags the forcing because most power is generated in the inboard slots. (d) Velocity into inboard slot versus phase and initial width. Contour interval 0.05 m/s. (e) Overall phase lag versus overall power output. Half-width is sampled at 0.25 m width (uppermost dots) and then at 0.125 m intervals up to 2.5 m (lowermost dots). Dot color corresponds to the fractional change in aperture during the tidal cycle. Thick black horizontal line shows phase lag relative to a fiducial model, gray lines show 1σ error in observed phase lag. Blue vertical lines show the observed power output of Enceladus; red lines include the additional power required for vaporization of gas escaping Enceladus.

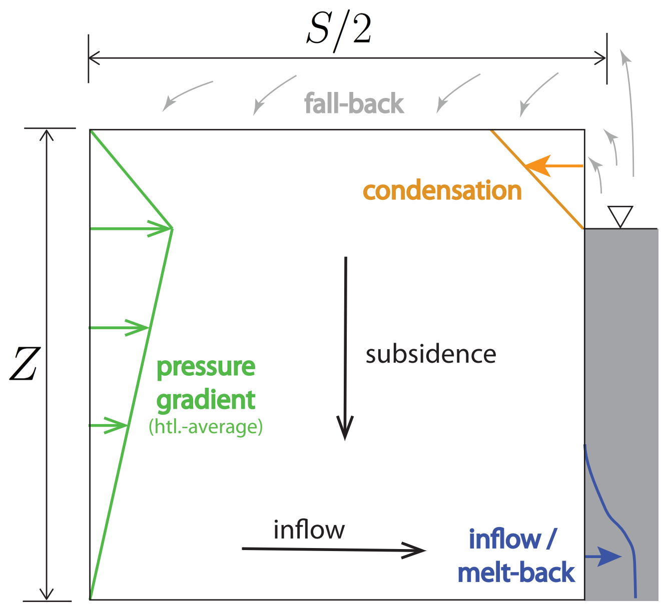

Figure S6. Add an up arrow to this slide. Long-lived liquid-water slots (that are in isostatic balance with adjacent ice) set up differential stresses that drive flow in the adjacent ice shell. Removal of ice by inflow and slot melt-back is compensated by subsidence. Subsidence provides accommodation space for condensation of vapor and for ballistic fall-back of geysered ice particles (materials that would otherwise seal the slot, powering down the eruptions).

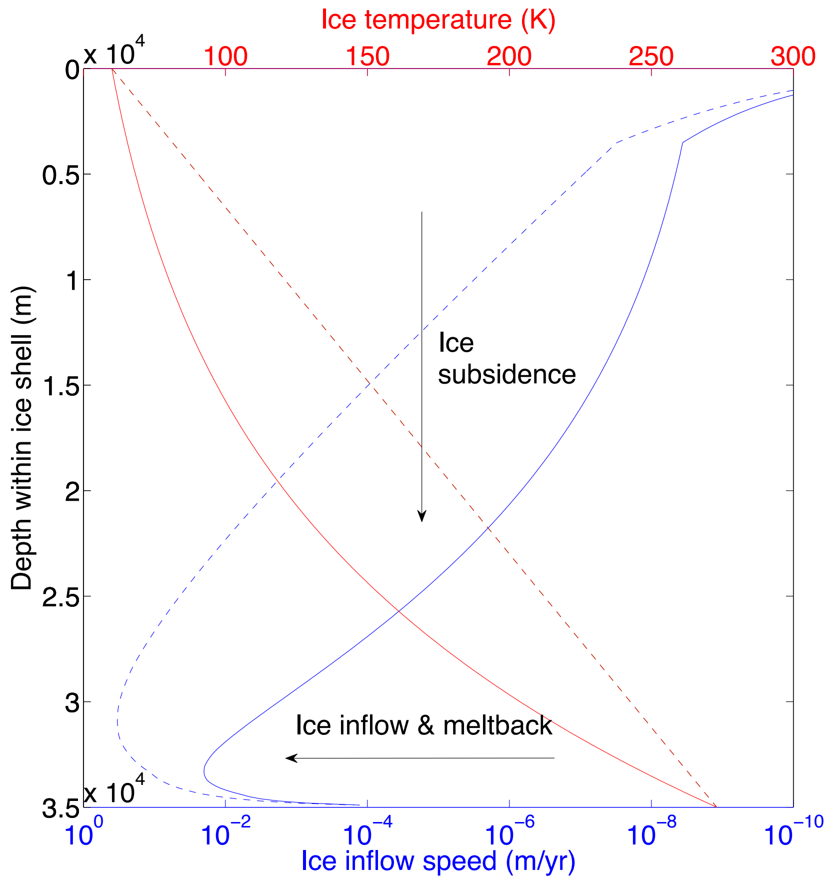

Figure S7. Diagram to show how long-lived water-filled slots affect ice shell tectonics. Assuming an initially-conductive thermal profile within the shell (dashed red line), ice will flow viscously into the slot (dashed blue line), driven by the stress difference between the shell and the slot (Fig. S6). The removal of material from near the base of the ice shell causes subsidence of cold ice from above. This cools the lower shell, in turn reducing inflow. Mean ice inflow is reduced tenfold at equilibrium (solid lines).

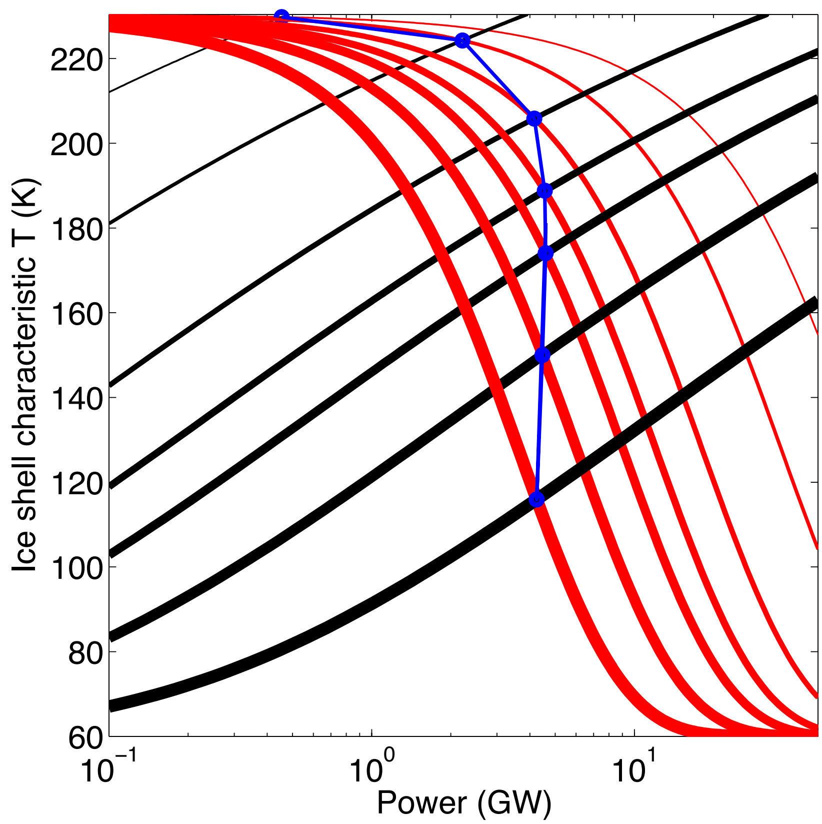

Figure S8. Equilibria for Enceladus' ice shell using long-lived water-filled slots as the boundary condition for a simple model of ice shell thermal feedbacks. The lines correspond to shell thicknesses of 5, 10, 20, 30, 40, 60, and 100 km (in order of increasing line thickness). The black lines show the mass fluxes of ice flowing into the slot as an increasing function of ice shell characteristic temperature (expressed as an equivalent latent heat flux, with units of power). The red lines show the temperatures for Enceladus' ice shell as a decreasing function of the increasing subsidence associated with the mass flux. The equilibrium for each ice shell thickness is shown by a blue circle. The blue line connecting the blue circles shows how equilibrium power output plateaus and then slightly declines with increasing ice shell thickness. A correction is made for increased shell-averaged gravity as shell thickness increases.

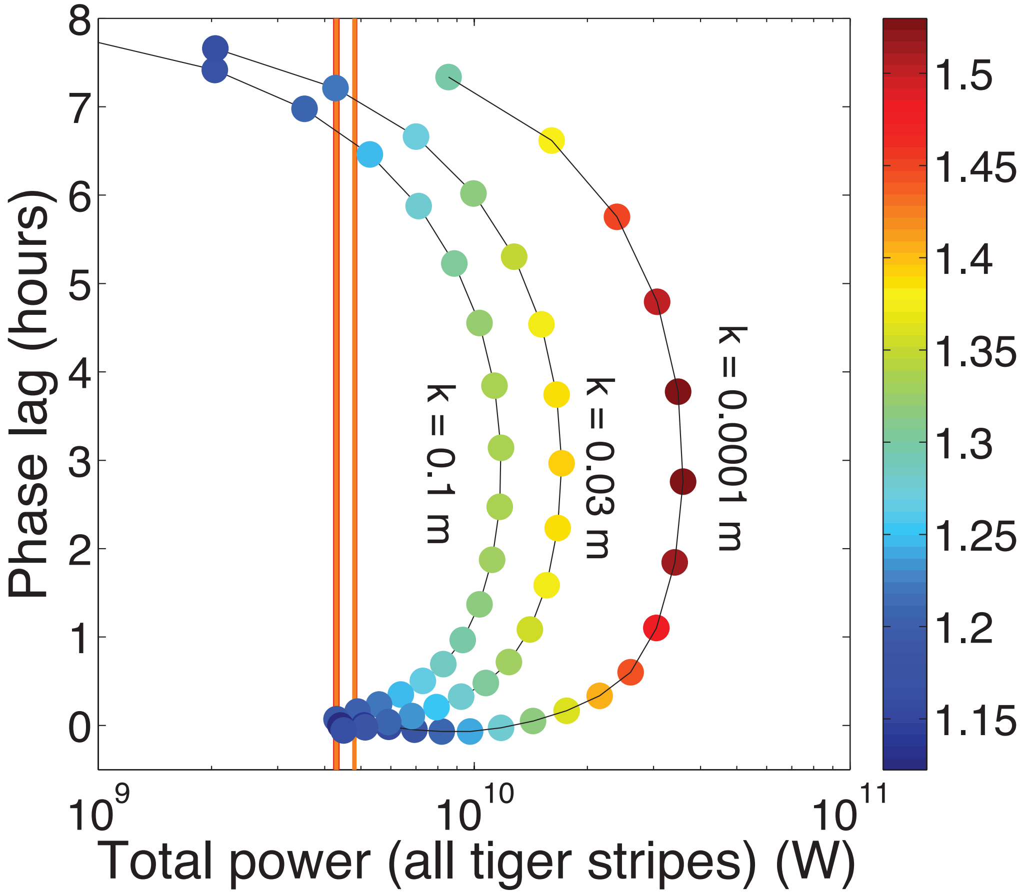

Figure S9. Sensitivity of power to k (roughness). Assuming two outboard slots with $L_{ob} = 151$ km, and two inboard slots with $L_{ib} = 93$ km. **(Need to add additional drag term here).** Dot color corresponds to the fractional change in aperture during the tidal cycle. Orange vertical lines show the observed power output of Enceladus, including the additional power required for vaporization of gas escaping Enceladus.

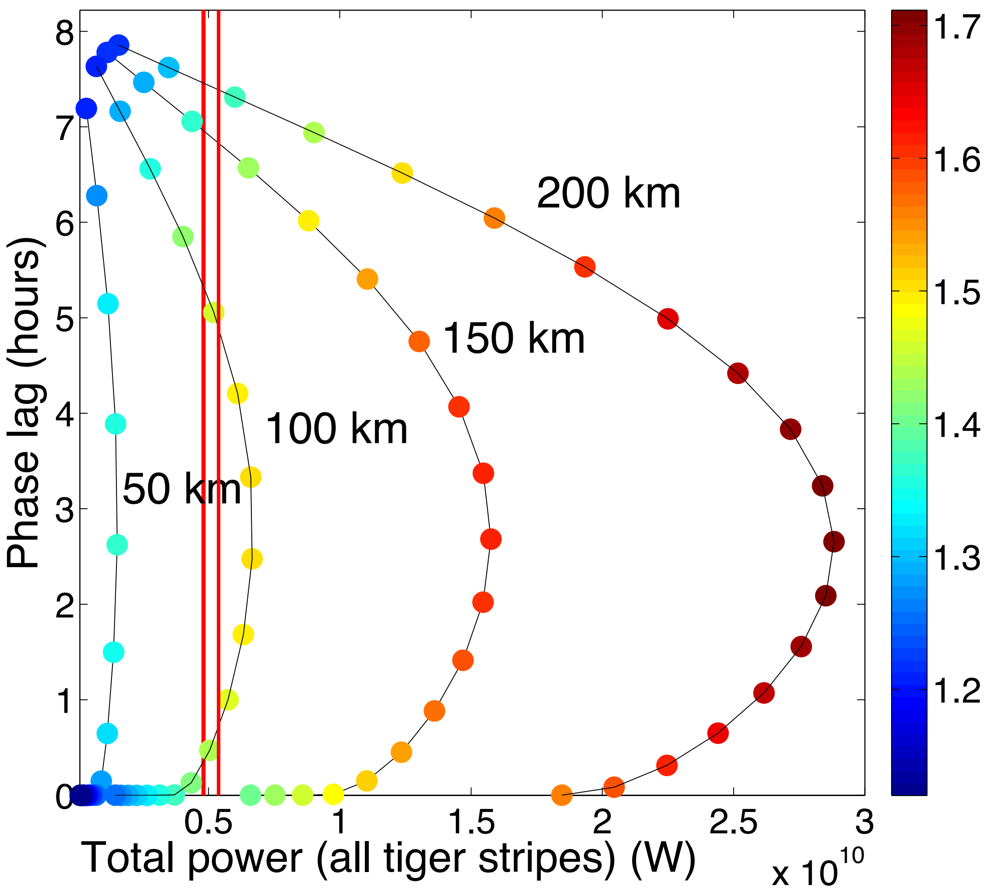

Figure S10. Sensitivity of power to L, considering non-interacting equal-length slots. Dot color corresponds to the fractional change in aperture during the tidal cycle. Orange vertical lines show the observed power output of Enceladus; red lines include the additional power required for vaporization of gas escaping Enceladus.